UNIVERSIDADE FEDERAL DO CEARÁ

CENTRO DE TECNOLOGIA

DEPARTAMENTO DE ENGENHARIA METALÚRGICA E DE MATERIAIS

CARLOS SAMUEL ALVES DA SILVA

IN-SITU TEXTURE ANALYSIS AND CRYSTALLOGRAPHIC ASPECTS OF PEARLITIC STEEL SUBJECTED TO PURE SHEAR IN UNIAXIAL STRESS

FORTALEZA

2023

CARLOS SAMUEL ALVES DASILVA

IN-SITU TEXTURE ANALYSIS AND CRYSTALLOGRAPHIC ASPECTS OF PEARLITIC STEEL SUBJECTED TO PURE SHEAR IN UNIAXIAL STRESS

Course Conclusion Paper presented to the Undergraduate Course in Mettalurgical Engineering at the Technology Center of the Federal University of Ceará, as a partial requeriment for obtain a Bachelo's degree in Metallurgical Engineering.

Advisor: Prof. Dr. Hamilton Ferreira Gomes de Abreu.

Co-advisor: Prof. Dr. Miloslav Béreš.

FORTALEZA

2023

Dados Internacionais de Catalogação na Publicação
Universidade Federal do Ceará
Sistema de Bibliotecas
Gerada automaticamente pelo módulo Catalog, mediante os dados fornecidos pelo(a) autor(a)

S579i Silva, Carlos Samuel Alves da.
In-situ texture analysis and crystallographic aspects of pearlitic steel subjected to pure shear in uniaxial stress / Carlos Samuel Alves da Silva. – 2023.
42 f. : il. color.

Trabalho de Conclusão de Curso (graduação) – Universidade Federal do Ceará, Centro de Tecnologia, Curso de Engenharia Metalúrgica, Fortaleza, 2023.
Orientação: Prof. Dr. Hamilton Ferreira Gomes de Abreu .

1. Pearlitic steel. 2. Texture. 3. In-situ synchrotron X-ray diffraction. 4. Pure shear. 5. In-situ texture. I. Título.

CDD 669

CARLOS SAMUEL ALVES DA SILVA

IN-SITU TEXTURE ANALYSIS AND CRYSTALLOGRAPHIC ASPECTS OF PEARLITIC STEEL SUBJECTED TO PURE SHEAR IN UNIAXIAL STRESS

Course Conclusion Paper presented to the Undergraduate Course in Mettalurgical Engineering at the Technology Center of the Federal University of Ceará, as a partial requeriment for obtain a Bachelo's degree in Metallurgical Engineering.

Approved on the 7th December, 2023

EXAMINING COMMISSION

_____

Prof. Dr. Hamilton Ferreira Gomes de Abreu
(Adivisor)Universidade Federal do Ceará (UFC)

_____

Prof. Dr. Miloslav Béreš.
(Co-Adivisor)Universidade Federal do Ceará (UFC)

_____

Prof. Dr. Cleiton Carvalho Silva
Universidade Federal do Ceará (UFC)

To my son, Luíz Pedro.

ACKNOWLEDFMENTS

To my parents, Maria and Reginaldo, who cared so much about their children's education, going to great lengths to provide us with educational opportunities. To my sister, Samea, for always being my best friend. To my grandparents, who taught me the path I should follow. To my uncles Josué and Carlos, who sometimes played the role of father so that I could continue my studies. I would like to express my sincere gratitude to my advisor, Professor Hamilton Ferreira Gomes de Abreu, for his encouragement and his immense contribution to this work. Thank you for believing in my work. I would also like to thank my co-supervisor, Professor Miloslav Béreš, for his immense support, sparing no effort to help me overcome the difficulties faced throughout this work. For always making all the necessary resources available to me on a consistent basis. Thank you for entrusting me with my responsibilities and for charging me whenever necessary. I would like to thank the Federal University of Ceará (UFC), especially the professors at the Department of Engineering and Metallurgical and Materials Science (DEMM). Special thanks to my friends, Dr.. Luis Flávio Gaspar Herculano and Professor Janaína Gonçaves Maria da Silva Machado. To the people at the Materials Characterization Laboratory (LACAM) - students, assistants. Thanks to the Central Analítica-UFC (funded by FINEP-CT-INFRA, CAPES-Pro-Equipamentos and MCTI-CNPq-SisNano2.0). To CNPq, for their financial support in maintaining my scholarship for several semesters. To the UFC laboratory: LACAM. To the PETRA III German Electron Synchrotron DESY (Hamburg/Germany), for data acquision. And finally, my mother-in-law Luci, my partner Eduarda and my son Luiz Pedro, who have supported and encouraged me over the last three years.

“He is not afraid of bad news; his heart is firm, trusting in the Lord”. (Psalm 112:7)

ABSTRACT

In-Situ synchrotron X-ray diffraction experiments were conducted on pearlitic steel sample with a carbon content of 0.74% by weight. Specimens were subjected to shear deformation in two-dimensional diffraction patterns were acquired during uniaxial loading to investigate the crystallographic changes. Rietveld refinement was used to analyze the evolution of Dislocation Density, Lattice Microstrain in the ferritic phase and the crystallographic texture was investigated in both phases. The analysis revealed that texture from $\{110\}\langle 113\rangle_{\alpha}$ component to $\{113\}\langle 121\rangle_{\alpha}$ component and then, stabilizing in $\{013\}\langle uvw\rangle_{\alpha}$ fiber components. The cementite showed a $\{100, 010, \text{and } 001\}_{\theta}$ texture planes and one strong preferential reorientation to planes close the same directions. Additionally, dislocation nucleation of interface α/θ promotes the amorphization of cementite and the activation of slip along non-compact directions in $\{310\}_{\alpha}$ planes due to meeting interfacial defects. The orthorhombic phase orientation limits the rotation in the α-BCC, does not possibility the accommodation of defects to activation new reflections more stable. The increase of Dislocation Density promoted by activation of slip systems in ferrite, contributes to the macroscopic hardening of the pearlite. The influence of microstructural changes on mechanical properties is discussed.

Keywords: Pearlitic Steel, Pure Shear Stress, *In-Situ* Texture of Cementite, *In-Situ* Synchrotron X-ray Diffraction.

RESUMO

Foram realizados experimentos de difração de raios-X em radiação sincrotron *In-Situ* em amostras de aço perlítico com teor de carbono de 0,74% em peso. As amostras foram submetidas à deformação por cisalhamento em padrões de difração bidimensionais adquiridos durante o carregamento uniaxial para investigar as alterações cristalográficas. O refinamento de Rietveld foi usado para analisar a evolução da densidade de discordâncias, da microdeformação da fase ferrítica, e também para a investigação da textura cristalográfica em ambas as fases. A análise revelou que a textura passou do componente $\{110\}\langle 113\rangle_{\alpha}$ para o componente $\{113\}\langle 121\rangle_{\alpha}$ e, em seguida, estabilizou-se nos componentes de fibra $\{013\}\langle uvw\rangle_{\alpha}$. A cementita apresentou planos de textura $\{100,\ 010,\ \text{and}\ 001\}_{\theta}$ e uma forte reorientação preferencial para planos próximos às mesmas direções. Além disso, a nucleação de discordâncias na interface α/θ promove a amorfização da cementita e a ativação de sistemas de deslizamento ao longo de direções não compactas nos planos $\{310\}_{\alpha}$ devido ao encontro de defeitos interfaciais. A orientação da fase ortorrômbica limita a rotação no α-BCC e não permite a acomodação de defeitos para a ativação de novas reflexões mais estáveis. O aumento na densidade de discordancia promovido pela ativação de sistemas de deslizamento na ferrita contribui para o encruamento da perlita. A influência das alterações microestruturais nas propriedades mecânicas é discutida.

Palavras-chave: Aço perlítico, tensão de cisalhamento puro, textura *In-Situ* da cementita, *In-Situ* síncrotron difração de raios-X.

LIST OF FIGURES

CONTENTS

1. INTRODUCTION

Pearlitic steels, constituting a remarkable category of metallic materials, play a crucial role in diverse industrial applications due to their unique mechanical properties. The distinctive microstructure, known as perlite, is formed by a ferritic matrix housing alternating layers of ferrite α-BCC and cementite θ-BOC, imparting exceptional characteristics crucial for variet industrial applications. Beyond its structural stability, perlite introduces a distinctive combination of toughness and hardness, providing significant resistance to crack propagation. This renders pearlitic steels prominent in scenarios where maintain structural integrity is paramount. Yet, devil deeper into the mechanical behavior of these steel, we explore additional critical factors that contribute to their overall performance.

The response to mechanical stress in pearlitic steels is intricately linked to the complex arrangement of phases present. Examining phenomena such as shear, where forces act parallel but in opposite directions within layers of pearlite, become essential. Understating shear mechanisms is integral to predicting and enhancing the material's resilience in applications subjected to de varied stress patterns how like friction or torsion stress (S. Suwas et al., 2019). Therefore, the phenomenon under study and the possibility of applying this morphology are perfectly associated with its use in breaking cables or wires for tensile reinforcement in flexible pipes for oil extraction.

With this, the dislocation density within the crystal lattice describes a role of the mechanical behavior of pearlitic steels. Dislocations, being defects in the crystal structure, significantly influence properties like strength and ductility. A nuanced exploration of dislocations density provides knowledge into the material's deformation mechanisms, aiding in the optimization of its mechanical response under different loading conditions. In parallel, the crystallographic texture of pearlitic steels, representing the preferred orientation of grains, and this can describe and determine the mechanical properties mentioned above. Because, variations in texture influence anisotropy, affect how the material responds to mechanical forces in different directions. Understating and manipulating crystallographic texture offer avenues for tailoring the mechanical behavior of perlitic steels to meet specific industrial requirements.

In this sense, to comprehensively explore the mechanical characteristic of pearlitic steels, we delve into advanced characterization techniques. X-ray diffraction (XRD) allows for detailed examination of the crystallographic structure, providing valuable information about, phase

fraction and grain orientation. Complementary, macro-texture studies, which investigate the orientation distribution of grains, offer insights into how these materials behave under different lading conditions. Moreover, Electron Backscatter Diffraction (EBSD) emerges as a powerfully tool for mapping crystallographic orientations as the micro scale. EBSD enables a detailed understanding of the material's microstructure, including grain boundary and defects. Additionally, investigating orientation relationship between different phases can be done with the TEM techniques and becomes crucial for predicting mechanical behavior under specific conditions.

Many authors [C. P. L. Rodrigo, 2021; M. Dollar, 1988; Vaibhav N. Khiratkar, 2021; Ning Guo, 2015; Jairo Alberto Muñoz, 2021; Mohammad Masoumi, 2022; Pablo B. P Leão et al, 2023) have research the failure of pearlitic steel and a few research's explain the crystallographic aspects (A. Mussi, 2016; H. K. D. H. Bhadeshia, 2018) of cementite phase. Still, no work has been developed to analyze the crystallographic behavior, with an *In-Situ* macro-texture of both phases. In this work, the mechanism to deformation of pearlitic steel was analyzed through specimens with uniaxial tension subjected to X-rays diffraction in transmission by Synchrotron light radiation. Additionally, the Scanning Electron Microscopy (SEM), Electron Backscatter Diffraction (EBSD), Transmition Electron Microscopy (TEM) and Transmission Electron Backscatter Diffraction (t-EBSD) techniques was employed. The lattice behavior, microstrain, dislocation density for ferritic phase and Macro Texture Evolution *In-Situ* for both phases is discussed

2. LITERATURE REVIEW

This pealitic steel, can achieve a yield stress of 700 MPa at 1600 MPa and an ultimate tensile stress of 1000 MPa at 2300 MPa. However, for drawn wires tested in laboratory conditions, a stress of approximately 7 GPa was recorded (Steffen Scherbring, 2024; Lichu Zhou, 2022; Yujiao Li, 2014). Below, is the graphic (Fig. 1) with different situations of pearlitic steel shows the stress x strain mechanical properties.

Figure 1 - Engineering tensile stress-strain curves for the different pearlitic steel wires.

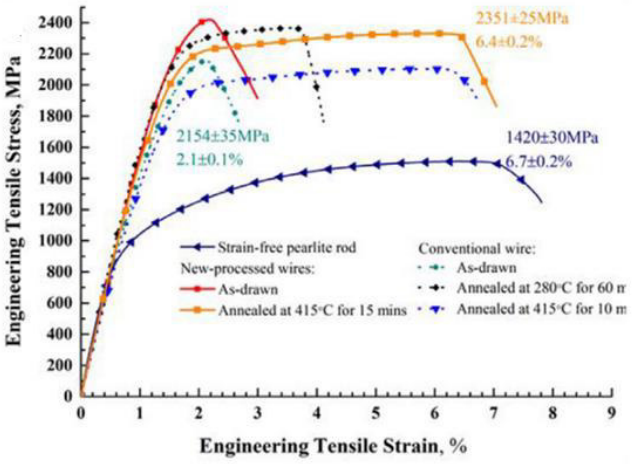

Source: Edited from Lichu Zhou (2022).

Of course, these properties are linked to its morphological characteristics such as grain size, size of pearlite colonies, previous austenite, spacing and shape of cementite lamellae (A.M. Elwazri, 2005; T. Shinozaki, 2006; C. Lei, 2007; Lichu Zhou, 2022). Thus, the managing these characteristics can provide applicability, for example, bridge cables and frames for oil extraction industry.

In this sense, the influence of both phases on strain hardening was researched for different types of deformation (Vaibhav N. Khiratkar, 2021; Habib Sidhom, 2015). With torsion and tensile loading, they showed that coarse and fine pearlite will influence the misorientation between interlamellar spacings and fracture behavior. To Confirms the importance of lamellar morphology, H. P. L. Pedro (2023), showed in X-rays analysis, that spheroidized (globular) cementite will accumulate less deformation than mixed (globular and lamellar) morphology. That happens because the cementite lamellar will pile-up at interfacial defects, preventing the

movement of dislocations, contributing to strain hardening (Ning Guo, 2015). In the Fig.2 is the deformed pearlite, with the shear bands highlighted. As can be seen, the microstructure consists of alternating cementite lamellae with an orthorhombic structure bathed in a body-centered cubic ferritic matrix.

Figure 2 - Heterogeneous deformation generated by tensile loading.

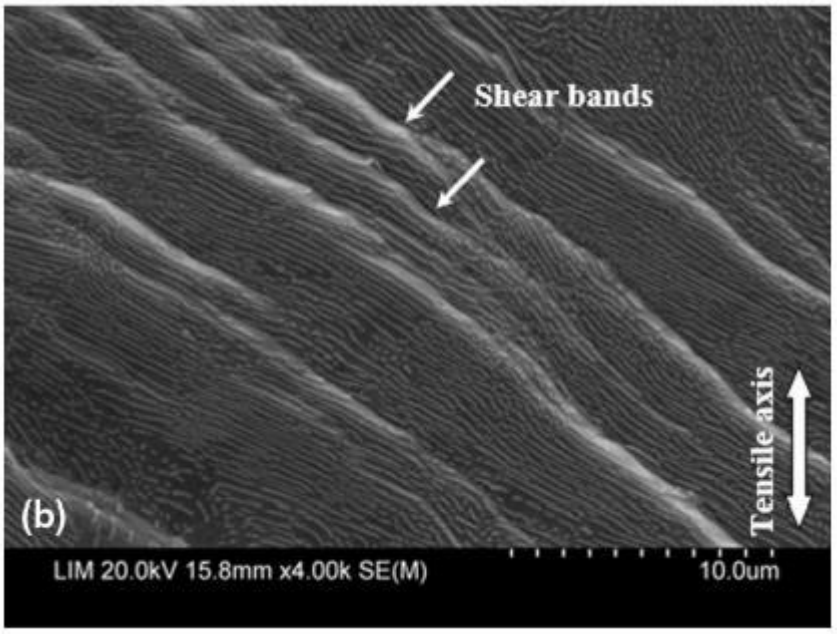

Source: from Habib Sidhom (2015)

Previous TEM analysis has already reported that ferrite it is responsible for control work hardening in pearlite, and fracture will occur to higher stress values with the breakage of cementite plates (M. Dollar, 1988). Additionally, in *In-Situ* diffraction, M. L. Young (2007) (Neutron and Synchrotron) and E. Gadalińska (2020) (Synchrotron), in analyzing lattice parameter behavior, showed that both phases are similar in elastic properties and the ferrite will transfer load to cementite, explain that, due your hardness, the orthorhombic phase is elastically deformed until failure. Also with *In-Situ* diffraction studies for hypereutectoid compositions, it was possible to find an amorphization in the cementite phase with true strain evolution (Akira Taniyama, 2017). This factor arises from cementite decomposition that contributes to annihilate the interfacial dislocations (Y. T. Zhou, 2022). In Fig. 3a-b it is possible see the failure of cementite and the amorphization to higher deformations.

Figure 3 - (a) TEM bright field with the shear band and the interfacial defects in interphase boundary (b) a HRTEM shows the lamellae of cementite with the amorphous pattern to high deformation.

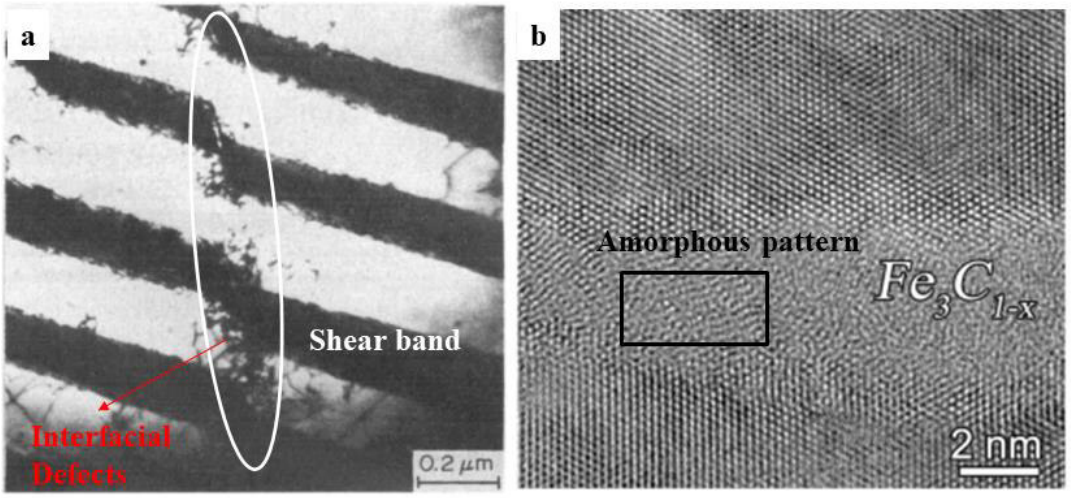

Source: modify of M. Dollar (1987) and modify of Y. T. Zhou (2022).

Nonetheless, all interactions between phases, have a direct connection with the preferred orientations between them. Pablo B. P Leão et al., (2023) conducted the Digital Image Correlation in fully pearlitic steel, showing that strain concentration occurs in the colony with parallel to the tensile direction. The same author, Pablo B. P Leão et al., (2023), but in another work with the crystallographic texture, reported that cracks and micro-cracks will nucleate between small recrystallized grains inside the $\{111\} < 112 >$ pearlitic blocks. Mohammad Masoumi et al., (2020), Jairo Alberto Muñoz (2021) and H. P. L. Pedro (2023) separately, with texture analysis, shows that the cold work in pearlitic steel can increase of crystallographic defects, promoting the formation of ferritic/pearlitic sub-grains, increasing the mechanical resistance due the less mobility of dislocations.

With this in mind, C. P. L. Rodrigo (2021) in study of failure by environmentally assisted cracking, suggested that, the refined microstructure prevents growth and can deflect crack, maintaining free propagation to $(223)[1\bar{1}0]$ and $(\bar{1}11)[1\bar{1}2]$. It is clear that the mean free path of dislocation will be influenced by lamellae morphology/crystallinity and the size of sub-grain following the classical Hall-Petch relationship (Equation 1) (Jairo Alberto Muñoz, 2021; H. P. L. Pedro 2023; Pablo B. P Leão et al., 2023; E. Gadalińska, 2020; C. P. L. Rodrigo, 2021),

$$\tau = \tau^{\circ} + \frac{k}{\sqrt{d}} \qquad (1)$$

where, k is the Hall-Petch constant, d is grain size, $\tau°$ is the friction shear stress to move a dislocation, and τ is shear stress (C.S. Pande, 2009; George E. Dieter, 1981).

Despite the influence of cementite deformation in pearlitic steel being widely studied, the crystallographic behavior is still unknown due to the high complexity of the structure. Giving a structural and crystallographic characterization, H. K. D. H. Bhadeshia (2018) elucidates that the orthorhombic structure can develop defects such as dislocations, faults and vacancies, and score another's physical properties. E. Gadalińska (2020) using modeling and compare with experimental data, found the Young modulus (E_{hkl}) of cementite to be between 160-260 GPa and 220 GPa for pearlite. However, with different volumes of unit cell Fe_3C (Pnma) and pressures, values were calculated between 174 GPa and 276 GPa for the Young modulus (E_{hkl}) and 74 GPa at 106 GPa for the Shear modulus (G_{hkl}) (M, Nikolussi, 2008). The Poisson's ratios were measured as 0.33 and 0,35 (v) (M. L. Young, 2007; H. K. D. H. Bhadeshia, 2018).

With these mechanical properties, given the plastic anisotropy of cementite, the morphology of the pearlitic microstructure has great importance for strain hardening (A. Mussi, 2016). Discussing about five ORs (Bagaryatsky, Isaichev, Pitsch–Petch, Near Bagaryatsky and Near Pitsch–Petch), K. Jaemin (2016), shows that, depending on the interfacial formation energy, misfits of dislocations will change. Therefore, the dislocation motion of the orthorhombic phase, also depends on the nucleation of interfacial defects in the ferrite/cementite boundary. This strain hardening in the interface of phases will give the energy to activation slip systems in ferrite and promote crystallographic changes to cementite (Akira Taniyama, 2017; Y. T Zhou, 2022; Changyu Wang, 2022; Lun-Wei_Liang et al., 2020 and 2023).

3. MATERIALS AND METHODS

The material used in this study was AISI 1075 pearlitic steel sheet 7 mm in thickness. A heat treatment at 1200 °C to austenite solubilization and colling with 1°C/second was conducted. From heat treated steel, samples with dimensions in Fig. 1a were extracted using an electric discharge machine. The chemical was obtained Optical Emission Spectroscopy Spectrometer, model PDA 7000. The determined chemical composition was 0.74C-0.65Mn-0.27Si-0.18Cr-(Bal)Fe.

In-Situ synchrotron x-ray diffraction measurements (SXRD) were conducted by the PETRA III Deutsche Elecktronen-Synchrotron DESY (Hamburg/Germany), with an energy of 86 kev which corresponds to a wavelength of 0.144 Ångström. A Beam size of 0.7 mm x 0.7 mm was used to acquire Debye-Scherrer diffraction rings using a Perkin Elmer amorphous silicon two-dimensional detector rings using a resolution of 200 µm x 200 µm, with sample to detector distance of 1220 mm. For calibration of the experimental setup and to determine instrumental values, a LaB_6 powder standard (NIST SRM660) was used.

Figure 4 - (a) The shear sample with the dimensions and the (b) test scheme for acquiring *In-Situ* diffraction patterns.

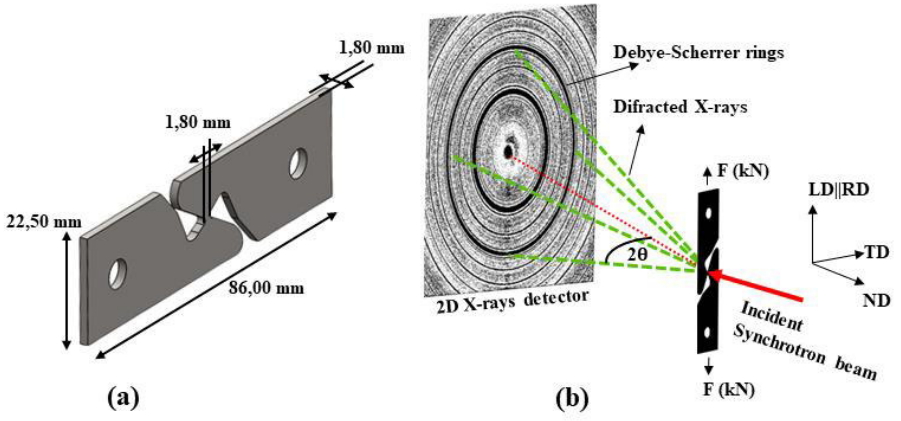

Source: Own elaboration.

The acquired data, were analyzed using GSAS-II software applying Rietveld method refinement (R. A. Young, 1993). With the refinement it was possible to estimate the incomplete pole figures through the series of harmonical coefficients modeling (V. Randle, 2010; S. Suwas

et al., 2014; H.J. Bunge et al., 1982 and 1993) (Equation 2).

$$A(\psi,\gamma,\phi,\beta) = 1 + \sum_{l=2}^{Nl} \frac{4\pi}{2l+1} \sum_{m=-l}^{l} \sum_{n=-l}^{l} C_l^{mn} k_l^m(\psi,\gamma) k_l^n(\phi,\beta) \quad (2)$$

In this equation, the two harmonic terms $k_l^m(\psi,\gamma)$ and $k_l^n(\phi,\beta)$ are measured by sample and crystal symmetry, respectively and C_l^{mn} are tabulated Harmonical Coefficients. Both harmonic terms sample coordinates estimated by diffractometer and crystal reflection coordinates determined by reflections $\{hkl\}$ (R. B. Von Dreele, 1997). These pole figures were transferred to the MTex open-source program MatLab toolbox through an algorithm that was used to calculate the ODFs (Orientations Distribution Functions). The calculated ODFs were compared with ODFs obtained from EBSD maps. For further details concerning this analysis, the reader is referred to references (Zifan Wang, 2022; Dan-dan Ma, 2020).

The lattice spacing obtained was used to determine value the of Burgers vectors (b) and the obtained value was applied in calculation of Shear Friction Stress ($\tau°$) by Peierls-Nabarro (Equation 3).

$$\tau° \approx \frac{2G}{1-v} e^{-\left[\frac{2\pi}{(1-v)b}\right]} \quad (3)$$

where (G) is calculated Shear Modulus using Hook's law for low deformation values and $v = 0.33$ is Poisson's ratio.

The Dislocation Density evolution (ρ) derived from (Equation 4), where the values of activation slip systems were analyzed, and the Shear Friction Stress ($\tau°$) and magnitude of Buggers vector (b) for each family plane were employed (George E. Dieter, 1981),

$$\tau = \tau° + \alpha G b M_{ODF} \sqrt{\rho} \quad (4)$$

were $\alpha = 0.3$ is a dislocation hardening constant and $M_{ODF} = 2.57$ is the average Taylor factor calculated using with three more intense ODF's components in initial state. Obtained values are similar to that described in literature for BCC materials (William F. Hosford et al., 1993 and 2010). Value obtained for the EBSD map in undeformed state was $M_{EBSD} = 2.8$. The slip

system was applied using the pure shear tensor (Christian Thiel, 2019).

The Full Width at Half Maximum was estimated from the Pseudo-Voigth function and then Lattice Microstrain values (ε) for α-BCC ferrite, were estimated using the Stokes and Wilson Method (Equation 4).

$$\varepsilon = \frac{\beta . \cos(\pi/180)}{4 . \sin(\pi/180)} \tag{4}$$

where (β), is the Full Width at Half Maximum and ($\pi/180$) is the Bragg Angle in radians (R. A. Young, 1993; B. D. Cullity, 2001; Leonid V. Azároff, 1968).

Secondary electron (SE) micrographs and Electron Backscatter Electron Diffraction (EBSD) data were collected using FEI ® Quanta 450 and FEI ® Quanta 650 Scanning Electron Microscopes. S. Sample was prepared applying standard metallographic preparation procedure consisting of grinding and polishing. Then, a chemical etching with 2% Nital for 3 seconds and final polishing with colloidal silica for 30 minutes was used. EBSD maps were acquired with an accelerator voltage of 15 kV with a tilt angle of 70° degrees.

In addition samples for Transmission Electron Microscopy (TEM) were prepared by twin-jet electron-polishing. The sample preparation consisted of careful grinding to produce metallic foils with a thickness of 60 µm. From the foils, disc samples with 3 mm in diameter were cut. Finally, twin-jet electron-polishing using solution of 10% perchloric acid in ethanol at 15V was carried out utilizing Struers Tenupol 3 equipment. Prepared samples were examined using TEM model FEI ® Tecnai G2 S-Twin equipped with ASTAR system for EBSD data acquisition. The Electron Diffraction patterns, transmission Electron Backscatter Electron Diffraction and Transmission images used were acquired at 200 kV in bright field mode. The collected EBSD data were analyzed Channel 5 and MTex open-source program MatLab.

4. RESULTS

4.1. Shear Stress and Shear Strain

Fig.5 shows the True Shear Stress – True Shear Strain curve, indicating the Ultimate Shear Strength (τ_{max}). Consider the shape geometry of sample (Fig. 1a), stress is concentrated at a 45° degree of the uniaxial load, characterizing the pure shear load. The Shear Modulus can be calculated using Hooke's law ($\tau = G.\gamma$) with $G = 67.00\ GPa$ and the maximum Shear Stress (τ_{max}) closely matches those seen in carbon steels subjected to pure shear deformation for ECAP (Jairo Alberto Muñoz, 2021). The curve reveals three stages: stage I with short easy glide, II with hardening stage and an III for interfacial defects saturation stage. Three points between stages are highlighted. Around $\gamma_{true} = 0.06$ occurred the first activations, at $\gamma_{true} = 0.21$ the strain accommodation happened and $\gamma_{true} = 0.51$ the crack propagation. The explanations will be given together with macro-texture in section 4. These behavior account for the changes that happened in ODF evolution and explanation follow (Willian F. Hosford et al., 2010; George E. Dieter, 1981)

Figure 5 - The True Shear Stress and True Shear Strain with the sections describing the crystallographic interactions.

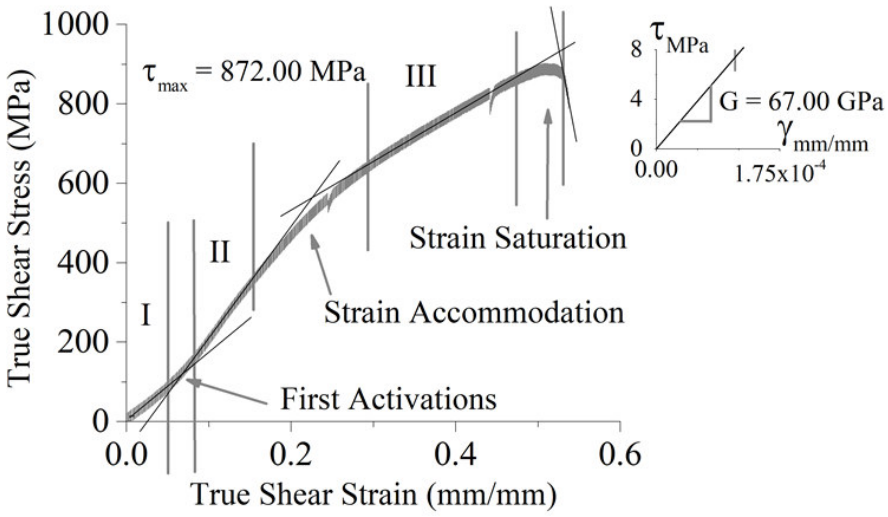

Source: Own elaboration.

4.2. Rietveld Refinement

The Rietveld refinement was performed on eight diffractograms, each representing significant change points during deformation (Fig. 6a). The initial data quality was $Rwp = 5.3\%$ corresponding to 94,7% parameter alignment, and two phases were quantified. Both phases, α-Ferrite ***(ICSD:9008536)*** and θ-Cementite ***(ICSD: 1008725)*** both clearly visible (Fig. 6b). However, when comparing the initial diffractogram with the last one in (Fig 6c), remarkable evolution in θ phase is evident. The peak width of the θ phase, increase during Shear deformation evolution particularly visible in the last diffractogram. Some reflection $\{102, 112\ and\ 211\}_\theta$ planes lose peak definition as do family planes around the $\{211\}_\alpha$ reflection. Considering the θ phase fraction (Fig. 6d) obtained through refinement Rietveld, it was initially 10.38%, decreasing to 3.8% in the final failure state.

Figure 6 - (a) and (b) Synchrotron X-Ray Diffractograms during true shear strain evolution, and initial data, respectively (c) enlarged profiles surround by base of peaks with initial and the last one data and (d) are the counts for phase fraction to θ phase.

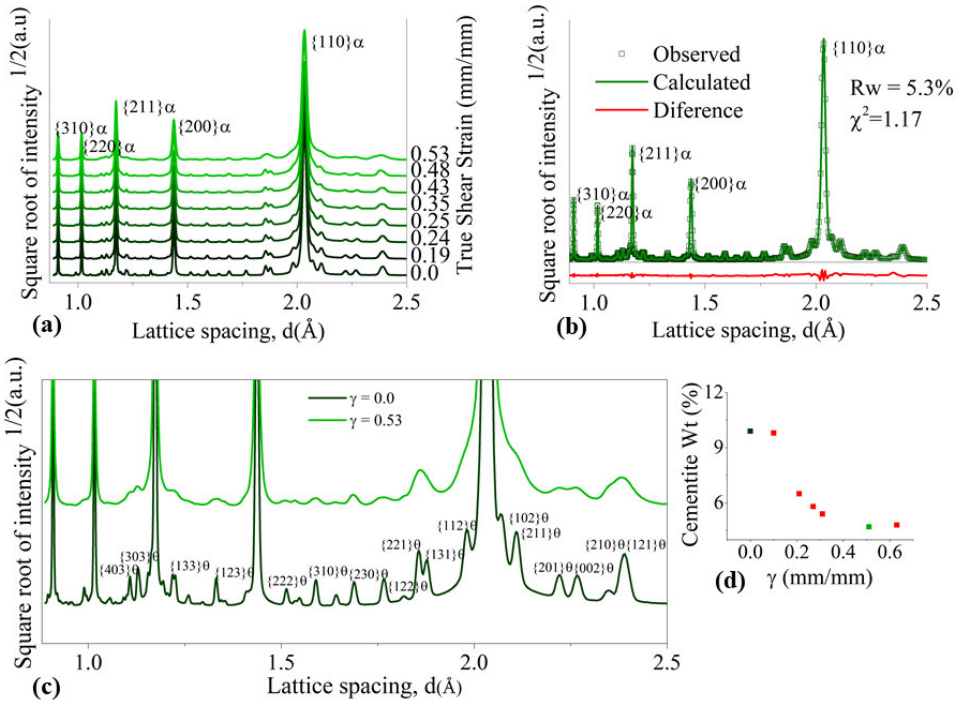

Source: Own elaboration.

4.3. FWHM (Full Width at Half Maximun), Lattice spacing, Microstrain and Dislocation Density *In-Situ*.

Fig. 7 displays the Full Width at Half Maximum (β), Dislocation Density (ρ), relative Lattice Spacing and relative Microstrain *In-Situ*. Notably, during True Shear Strain,there is a significant increase in β to $\{310\}_{\alpha}$ compared to the others five family planes (Fig. 7a). However, this outcome aligns with expectations for these family planes, as they exhibit a lower tendency to activate slip systems, due to their low atomic density. Considering this, the $\{110\}_{\alpha}$ family planes (Fig. 7b), show no significant change in β. Nevertheless, these planes activate slip systems, indicating a more pronounced alteration in Relative Lattice Spacing than others. The calculation involved the difference between the final d and initial $d°$ Lattice parameter.

Figure 7 - (a) Above the Full Width at Half Maximum and below the Dislocation density evolution during Shear deformation, (b) relative Lattice Spacing and relative Lattice Microstrain above and below respectively,(c) Dislocation Density evolution for {310, 113 and 321} family planes together the friction Shear Stress ($\tau°$).

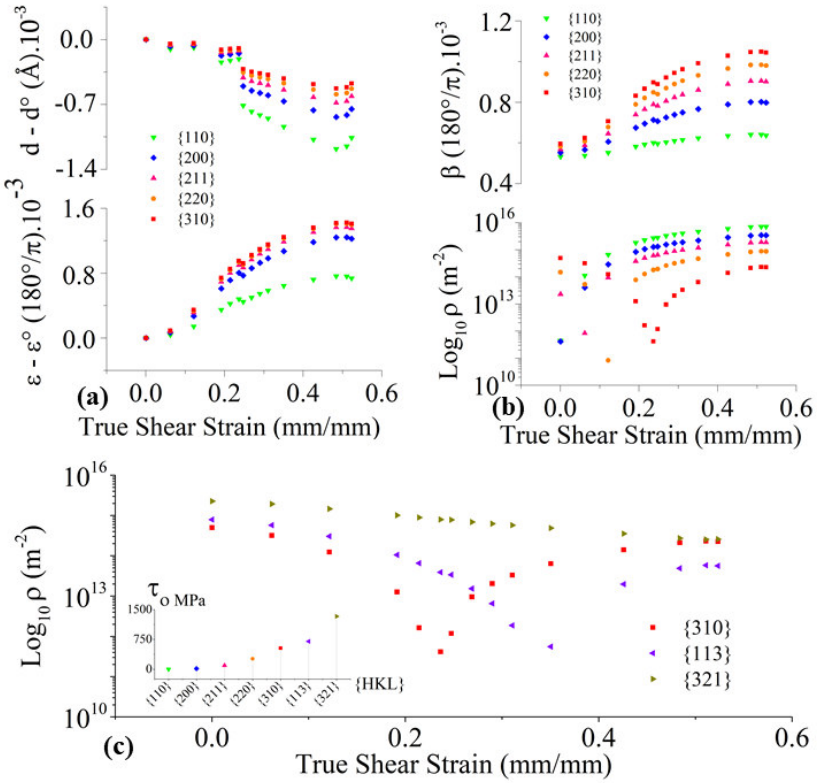

Source: Own elaboration.

The surge in the Lattice Microstrain values (Fig. 7b) becomes apparent in crystal planes with lower atomic density, increasing of up to $1.6x10^{-3}$ radians. The pronounced Dislocation Density (Fig.7 b-c) manifests more prominently in planes with higher atomic packing, exemplified by $\{110\ and\ 200\}_{\alpha}$ reflections, with magnitude ranging from $10^{13}\ m^{-2}$ to $10^{16}\ m^{-2}$. Some family planes, shows a decrease in the dislocation density between $\gamma_{true} = 0.20$ and $\gamma_{true} = 0.40$ and they are $\{310\ and\ 113\}$. It can be associated to activation of slip system and the explanations will be there in 5.1 section .It's worth to note that the values of dislocation increase with the lattice compression dynamics in relative lattice spacing (Fig. 7a).

The Dislocation Density (ρ) evolution and friction Shear Stress ($\tau°$) was measured across an others family planes that interacted in ODF's (Fig. 7c). In the initial state, the $\{113$ and $321\}_{\alpha}$ exhibited an accumulation of defects. These reflections have substantially higher frictional stress values $750\ MPa$ and $1500\ MPa$ respectively, than others family planes. The measurements for these planes, absent in the *In-Situ* reflections, were derived from calculated lattice parameter.

4.4. Crystallographic features of the tested sample and Synchrotron Macro-texture.

Figure 8 - (a) and (b) The IPF's (Z)//ND by Band Contrast map with undeformed and deformed region respectively, signaling a white circle the $< 001 >//ND$ reflection, (c) and (d) Kernel Average Misorientation maps following the graphics with Local Misorientation versus Frequency, (e) Bright Field -TEM image with the dislocation interface between lamellar of cementite and (f) Scanning Electron Microscopy (SEM) image with points of Shear Bands and the morphology of cementite after deformation.

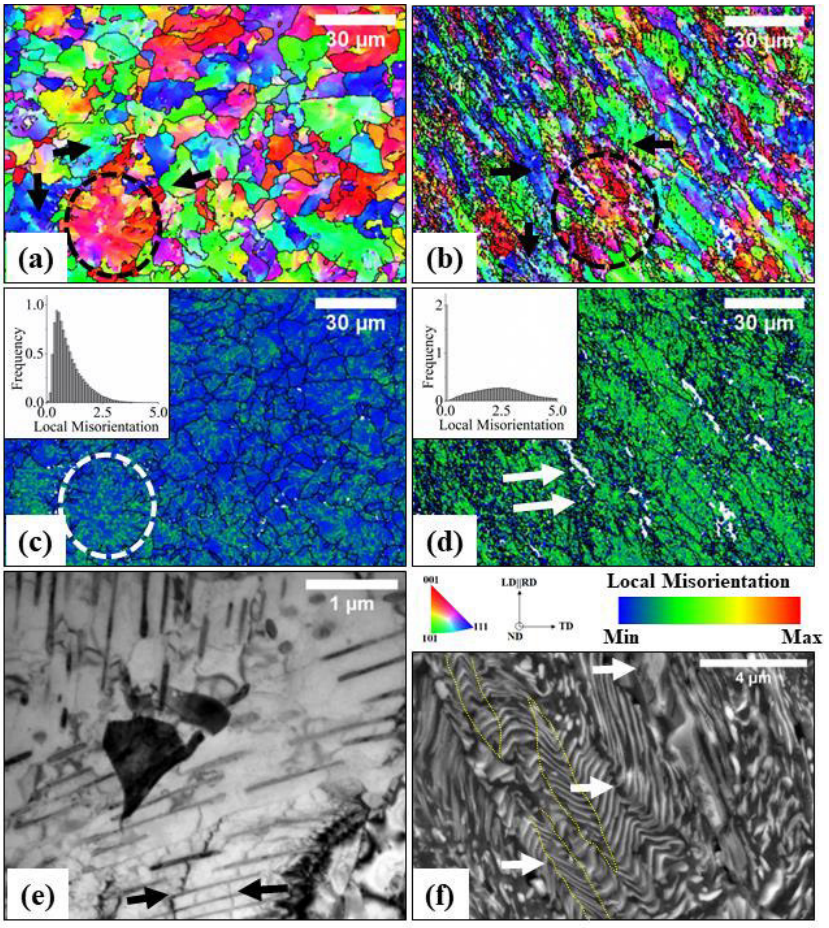

Source: Own elaboration.

Microstructural characterization was made in both deformed and unreformed situations. The Inverse Pole Figure is accounted for in (Fig. 8a-b), revealing fragmentation in reflections after deformation. These heterogeneities, form additional sub-reflections near the $< 112 >//ND$

and $< 102 >//ND$. The $< 110 >//ND$ reflection does not exhibit any sub-orientation, as well as minimal sub-directions in $< 111 >//ND$ have been observed. The analysis presented in (Fig. 8c-d), reveals that $< 001 >//ND$ reflection, before deformation, indicates a greater accumulation with low angle defects than $< 110 >//ND$ reflection. After deformation, the high fragmentation area with the $< 001, 102$ and $112 >//ND$ sub-reflections exhibits low misorientation. In Fig. 8e, the bright field TEM micrograph, illustrates the path of dislocation and a point of their meeting, following the $< uvw >//TD$. In this case, these defects will be moving perpendicular to the higher tension direction of the plane. Fig. 5f shows the bending of cementite below, in the middle, crack propagation in lamellar cementite perpendicular at shear band activation. The arrow above indicates a possible activation slip system on the cementite plate counter direction to the shear band (Fig. 8f).

Figure 9 - (a), (c) and (d) are the Bright Field TEM image, the phase map and Inverse Pole Figure map acquired by transmission Electron Backscatter Diffraction (t-EBSD) account α and θ phases. In (b) is the Selective Area Electron Diffraction (SAED) pattern with the Orientation Relationship between α/θ phases. The right side is the verification of the OR using the pole figures from t-EBSD.

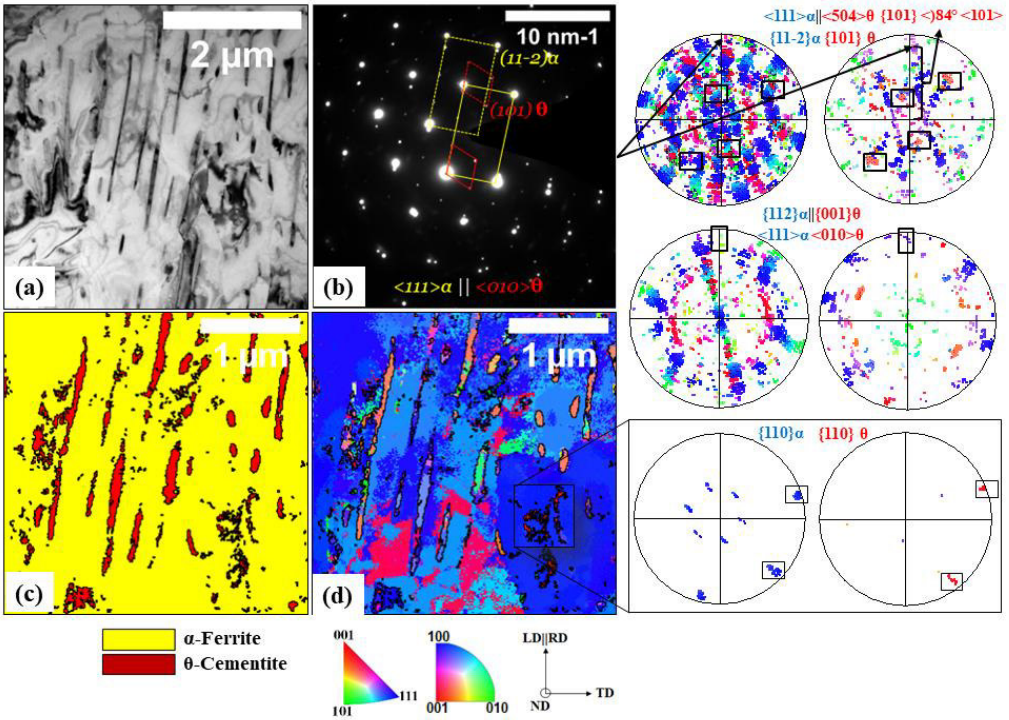

Source: Own elaboration.

The Transmission Electron Microscopy micrographs were analyzed to establish a starting point for the characterization of cementite macrotexture. The dislocation between cementite phase lamellae can be observed. It should be noted that defects align perpendicular to the lamellae, as shown in Fig. 8e, and both phases are accounted for in Fig. 9c. The SAED pattern revealed that the habit plane associated with the normal diffraction vector$< 111 >_{\alpha}//< 010 >_{\theta}$ is described to Isaichev Orientation Relationship, and correspond to $\{112\}_{\alpha}//\{001\}_{\theta}$. The correlation between the habit plane and texture was analyzed, with t-EBSD taken into account. It should also be noted that the $(101)_{\theta}$ plane is at an angle of 84° to the $[101]_{\theta}$ direction. In (Fig. 8d) a subset, is highlighted and the corresponding pole figures with $\{110\}//ND$ for each phase, these show the habit plane between $\{111\}_{\alpha}//\{001\}_{\theta}$ have the $< 110 >_{\alpha}//< 110 >_{\theta}//TD$. It is possible to have deviations between pole figure measurements due to cementite lattice parameters and transmission sample positioning. Section 2 explains how the transmission sample was acquired.

Figure 10 - *In-Situ* Synchrotron ODF's φ2 = 0° and 45° for α with the table components of right side and the legend below.

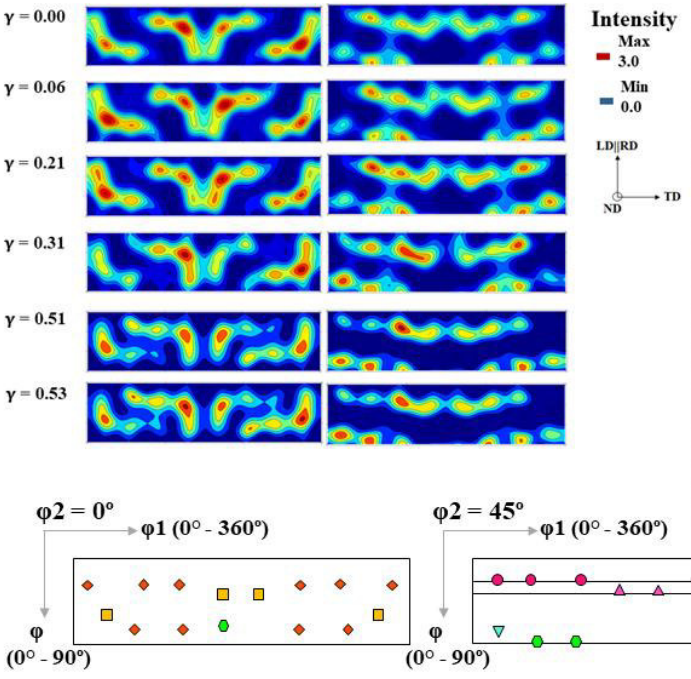

ODF's componentes for Fe

Component	φ1	ϕ	φ2	Symbol	HKL	UVW
1	10	17.5	0	◆	{310}	[15 -3 1]
2	112.5					[-1 -3 1]
3	247.5					[-1 3 -1]
4	350.5					[15 3 -1]
5	70.5					[1 -3 1]
6	290.5					[1 3 -1]
7	67.5	72.5				[1 -1 3]
8	292.5					[1 1 -3]
9	112.5					[-1 -1 3]
10	250.5					[-1 1 -3]
11	150	27.5		■	{210}	[-4 -2 1]
12	212.5					[-4 2 -1]
13	30	62.5				[4 -1 2]
14	330					[4 1 -2]
15	150	42.5		⬢	{110}	[-5 -2 2]
15	60	25	45	●	{113}	[-1 -5 2]
16	110					[-2 -1 1]
17	248					[1 2 -1]
18	295					[5 1 -2]
19	25					[2 -5 1]
20	140	35		▲	{112}	[-5 1 2]
21	218					[-1 5 -2]
22	56	90		⬢	{110}	[1 -1 2]
23	115					[-1 1 3]
24	245					[-1 1 -3]
25	294					[1 -1 -3]
26	22.5	74.5		▽	{123}	[1 -2 1]
27	342					[2 -1 -1]

Source: Own elaboration.

The crystallographic texture results for ODFs are depicted in figures (Fig. 10 and 11). These ODF's were calculated from incomplete pole figures obtained from the refinement through of the acquired patterns *In-Situ* explained in section 2. The legends are identified by symbols for both phases in the respective legends. The $\varphi 1$ range of $0°$ to $360°$ was chosen in both phases for its possibility to analyze all directions in the same family plane, because the sample does not have orthorhombic symmetry to shear deformation evolution (S. Suwas et al., 2019). The use of the family $\{hkl\}_\alpha$ notation was motivated by the symmetry of cubic crystals, whereas for $\{hkl\}_\theta$ the motivation was the symmetry in this particular phase which only permits the joining of planes with the same Miller indices order but different signal. The ODF's of α-ferrite, sections of $\varphi 2 = 0°, 45°$ were chosen, because in cubic crystals, they exhibit the major crystallographic interactions of interest. All directions to ODF in both phases were summarized at //TD, because the reference sample system. In Fig. 10, components interact during Shear Strain evolution for α-ferrite. Before $\gamma = 0.21$ the components only change the intensities, meaning the activation of the slip activated on existing system. In $\gamma = 0.31$ there are new components emerging with low intensities: $\{310\}[15\bar{3}1]//TD$ and $\{113\}[2\bar{5}1]//TD$. There are also some interactions for same $< 421 >//TD$ direction with distinct reflections. When the failure started ($\gamma = 0.51$), stabilization for $\{110, 113$ and $123\}$ fiber components occurs. The $\{310\}[15\bar{3}1]//TD$ become more intensities and emerging $\{310\}[15\ 3\bar{1}][\bar{1}\bar{1}3]$ and $[\bar{1}1\bar{3}]//TD$.

The θ-cementite were taken $\varphi 2 = 0°, 45°, 90°$ and $135°$ that's because, every interval $\varphi 2 = 180$, the ODF's sections are repeated and these sections summarized all major interaction components shown (Fig. 11). The $\varphi 2 = 135°$ has had changes in components directed at Transversal Direction and the $< uvw >$ close to then. Initially, the intensities in Synchrotron ODF's in secondary phase, accounted the same value with the α-ferrite and in ($\gamma = 0.51$), these up to 7.4. Follow the same perspective of the matrix interaction, at $\gamma = 0.21$, the θ only changes the intensities to the same directions $< uvw >$ with new reflections. It's interesting to note, this point the components$\{012\}[13\ 8\ \bar{4}]$, $\{023\}[\bar{4}3\bar{2}]$ $\varphi 2 = 0°$, $\{111\}[2\ 11\bar{13}]$ $\varphi 2 = 45°$, and $\{hkl\} < uvw >//TD$ $\varphi 2 = 135°$ are stable. The $\{100, 010$ and $001\}$ $< 14\ 9\ 0 >$ are close to same direction the stable components, decreases intensities with increasing deformation. These phenomena registered with the appearance of $\{310\}[15\bar{3}1]//TD$ and $\{113\}[2\bar{5}1]//TD$ in α-ferrite. For the $\gamma = 0.31$, the stable orientations explained above, go to more high intensities keeping this behavior at start failure in $\gamma = 0.51$.

Figure 11 - The the legend of $\varphi 2 = 0°, 45°, 90°$ and $135°$ showed the more intensity components of θ phase to *In-Situ* analysis. Below of the left side is the *In-Situ* Synchrotron calculated ODF Functions for θ during Shear Deformation Evolution. In the right side were comparing the initial and final ODF's components for α. The middle is the scheme of how the sub-reflection appears.

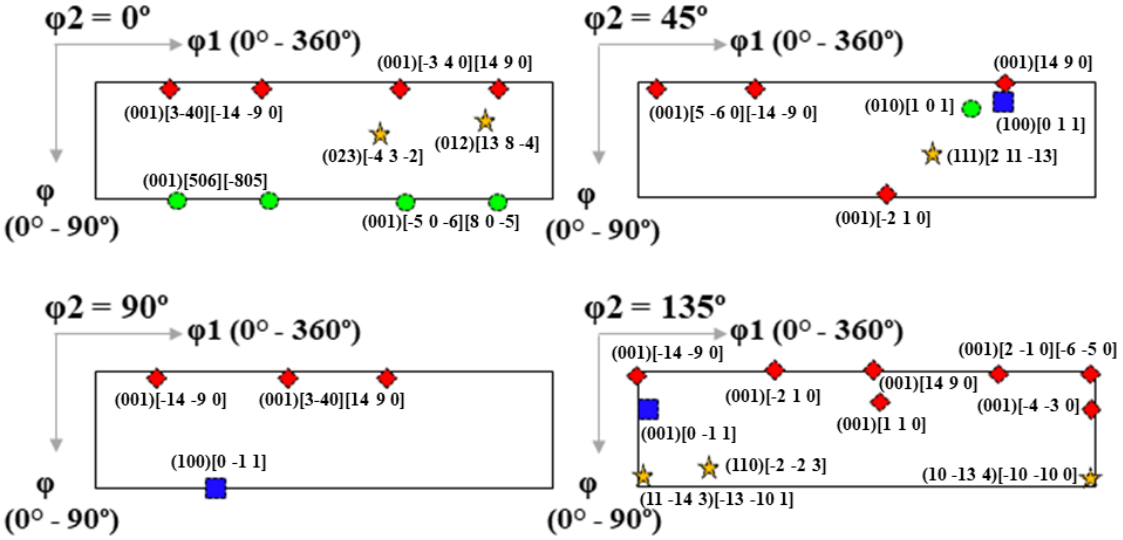

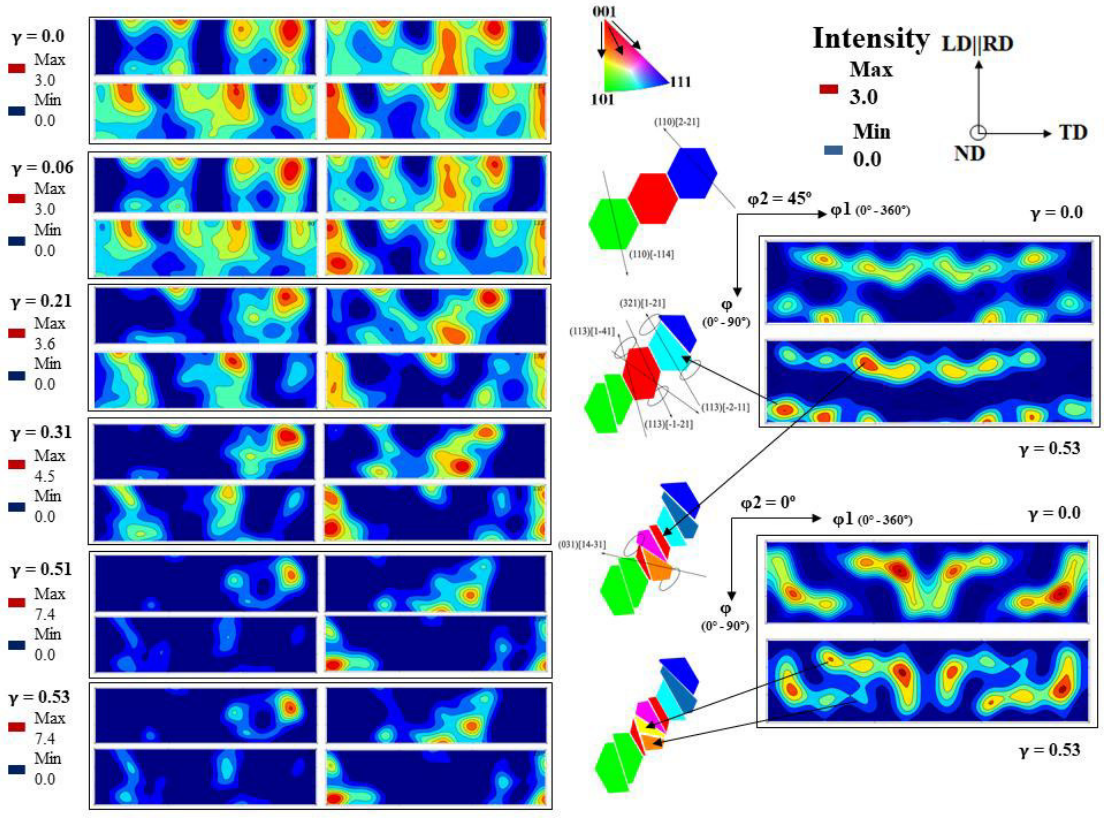

Source: Own elaboration.

5. DISCUSSIONS

5.1. Texture and crystallographic behavior of α-Ferrite

It is known that crystallographic texture can describe the entire thermal and/or mechanical history of metals through the tendency and changes in the preferential orientation crystals. In this aim, for the $\gamma = 0.0$, was found the $\{113\} < \text{uvw} >$ close to the $\{112\}$ fiber, the $\{110\} < 113 >< 112 >$ and $\{123\} < 121 >$ family components. Taking this into account, Y. Tian (2020) identified that rolling steel below the recrystallization temperature results in a strong $\{113\}$ and proximity to the $\{112\} < 110 >< 131 >$ orientation. Nevertheless, Mehdi Sanjari (2016) with quasi-*In-Situ* EBSD observed the same fiber $\{113\} < \text{uvw} >$, when studying the annealing in IF steels after cold rolling. These crystallographic behaviors were identified as a legacy of Cube texture after recrystallization (Ning Zhang, 2016). In addition, the $\{310\} < 113 >< 15\ 31 >$ were also described in Fig. 10. Nonetheless, Zhegnhua He (2023) showed in Fe-Ga alloy studies, the Goss texture $\{310\} < 001 >$ arise from the secondary recrystallization and Zhaoyue Liu (2022) shows the appearance of this texture kind in high-permeably grain-oriented silicon steel after annealing. However, Haitao Jiao (2020), presented in analysis with the cold rolling evolution the $\{013\} < 131 >$ also originating from a Cube texture. These facts summarizing that, the cold work process before recrystallization will influence the crystallographic texture, because the phase transformation texture comes from the prior austenite grain (R. K. Ray, 1990). All these interactions can be attributed to the interfaces between ferrite and previous the austenite grain, which change in the portion of ferrite, preserving the history of the crystallographic transformation in austenite portion. These discussions, arises only the initial state for the sample study and it denotes that the material underwent a recrystallization process, and as was normalized.

Addressing the texture evolution in α, $\gamma = 0.06$, were only change the intensities for the same components occur and this can be linked with the firsts activation slip system Fig. 5. The activation also occurs in slip systems normal to ND how like {113}<121> and {210}<131> family planes with the opposite direction. These activations will be occur together the {110}<113> and {112}<152>. The Relative Microstrain shows that {310} a reflection has a greater accumulation of deformations than others. In addition, the dislocation density before deformation in {113}, {310} and {321} shows a possible pre-hardening in these specific orientations Fig. 7a-c. Nonetheless, theses reflections have low atomic density, the frictions

stress to move a dislocation (activation of slip system) will too higher (Fig. 7c), the activations will depend on the direction of the component to α (C. Du, 2018; Toshihiko Teshima, 2017). If the stress component for that direction is very high, the only plausible explanation for the activation slip system with low Schmid Factor is, the existence of energy accumulated by rolling process occurring in the prior austenite portion. Thus being able activates the systems with different shear stress component (Pablo B.P. Leão et al., 2023).

However, analyzing the Fig. 8, the shear deformation will conserve the <110> directions in α and the $< 001 >//ND$ and $< 111 >//ND$ will be rotate to $< 013 >//ND$, $< 113 >//ND$, $< 123 >//ND$. In Fig. 10 in $\gamma = 0.21$ at $\gamma = 0.31$ it's possible to see the $\varphi 2 = 0°$ components $\{210\} < 421 >$ close to the $\{310\} < 131 >$ generating a new $\{110\} < 522 >$ component and $\varphi 2 = 45°$, the $\{113\} < 152 >$ go to $\{112\} < 152 >$. This rotation happens precisely in final of stage II when strain hardening is maximum and in the beginning Strain Accommodation region of Fig. 5. This happened because all energy (defects) acquired during stage II of strain hardening will accommodate according to the normal direction $< uvw >$ the {hkl} reflection, rotating the grain in the same or close $< uvw >$ to another $\{hkl\}'$ dissipating these energy with activation slip system, the Fig. 11 shows how this interaction occurs. To corroborate of this result, M. Mohammad et al (2022) analyzing the texture of pearlitic steels, reported the $\{112\}$ reflections, rotate for more atomically dense reflections. H. P. L. Pedro (2023) with bending spheroidized pearlitic steel the reduction of (001) fiber resulting a higher mechanical resistance.

Nonetheless, analyzing the same behavior before $\gamma = 0.31$ to another's components in Fig. 10, the interaction of $\{123\}[1\bar{2}1]$ and $\{123\}[2\bar{1}\bar{1}]$ shows the activation for these systems during accommodation of defects provides by the accommodation of interfacial defects. However, the magnitude of activated slip systems (Fig. 7c) shows a little decrease to {321} and {123}<112> there was an enlargement and approximation of the {110}<112> component ($\gamma = 0.51\ and\ 0.53$) in Fig 10. This late activation and accommodation of defects in stage III is due to you higher friction stress. For that, immediately after activation, the interfacial defects will go give the energy to rotate the grain and the dislocation will follow $\{123\}[1\bar{2}1]$ to $\{110\}[1\bar{1}2]$ (same direction) thus accounting for the lower values dislocations of {321} slip systems. Studies carried out by Anik H.M. Faisal and Christopher R. Weinberger (2023), with simulation to BCC crystals shows that the twins grow with stress relief, in other words, the interfacial defects will be energy to activation slip systems. The {112}<152> become again to

{113}<152> and the dislocation density go to higher after $\gamma = 0.35$ for {113} reflection (Fig. 7c). Ning Guo et al (2014) showed that during torsion of wires that, the shear stress will cause the change of orientations and then with increasing number of torsion revolutions, the intensity of that texture will decrease to <110> fiber, returning to primary orientation.

In addition, a different way for dislocations were to stage III, the hardening of perlite change the direction of {310}<113> to {310}<15 3 1> and this uncommon change indicates the high fragmentation grain. These small grains were described initially in Fig. 8b-d arise due to the activation of systems within sub grains originated from shear bands how like describe in the scheme of Fig. 10. The change of direction has a great influence of mean free path and interfacial defects to failure of pearlitic steel. P. Leão et al (2023) shows that the high fragmentation grain has low concentration of interfacial defects and they will align with the shear direction. Nonetheless Y. Yasuda (2018), proved that to component with small Schmid Factor and mean free path will have higher rates of strain-hardening. In studies with line broadening, Fuling Jiang (2019) showed of that increase of deformation, small grains will be sutured homogeneously of dislocations and heterogeneous pattern will arises with deformation evolution.

What was observed in this aim is the rotations and activations of sub-orientations coming from shear bands will generate highly hardened sub-grains how can be seen in the Fig. 8d with arrows. Therefore, follow the Hall-Petch effect, these sub-grains will be saturated with interfacial defects and with this, they will change the direction generating the high angle misorientation. Because this the change of new direction appears more strongly after of stage III in $\gamma = 0.51$ and 53 to α phase. The strain saturation will undergo when these sub grains nucleate more strain due your high strain hardening. In studies to cracking failure of pearlitic steel reported that the refined microstructure prevents crack growth and deflect propagation (C. P. L. Rodrigo, 2021). However, during shear evolution, the interface between the sub grains contains grater accumulated energy, these boundary will change the direction of sub-grain for align the strain of heterogeneous shape in sub-grain boundary. In another words, the change of direction {310}<113> to same {310}<1531> fiber indicate that the α structure will nucleate a crack as a way of relief strain energy. Because of this factor, the crack grows follow the grain boundary path how likes reported by P. Leão et al (2023).

5.2. Influence of cementite to strain-hardening

Despite the structure of cementite it has been explored for decades, the macro-texture, still needs to be refined. The analysis in SAED pattern reveal the Isaichev Orientation Relationship between α/θ were $< 111 > \alpha || < 010 > \theta$ with the $\{112\}_{\alpha}||\{101\}_{\theta}$ were find. This OR, brings with it a diffusion mechanism and consequently the thermal and/or mechanical process history (Y.T. Zhou, 2022; D.S. Zhou, 1992). The analysis for t-EBSD with the pole figures, reveal a different OR when used the same reference of SAED. Even with the difference between analysis, this allowed find the mostly slip systems for the θ, these being belonging $\{100, 010\ and\ 001\}$ family planes (H.K.D.H. Bhadeshia, 2020; A. Mussi, 2016). Observing the behavior of the θ ODF's in left side of Fig. 11, little activations of the slip systems were see in the first activation stage for α. Probably these little activation occurs due the low deformation capacity in plates of cementite how can be seen in the Fig. 8f. However, $\gamma = 0.06$, the sections of $\varphi 2 = 45°, 90°\ and\ 135°$, shows the tendency of the components retract to $\{001\ and\ 100\}$ family components for the close $< uvw >$, showing the same behavior of ferrite during strain accommodation (Fig. 10).

The Already M. Dollar (1988) shows that the fracture process will be determined by pearlite colonies with lamellae parallel to axis tensile and with the *In-Situ* SEM tensile test. Habib Sidhom (2015) shows the same perspective, noted that the lamellae normal to slip activation will incline to the tensile axis by heterogeneous deformation and the coarse lamellae will be fracture to first activations in ferrite. Unlike the α phase, which reorients with the same $< uvw >$ to accommodate interfacial defects after the strain-hardening, the θ phase will be present the same behavior as consequence of activation α systems. Nonetheless, the change of components for those with higher stress component in θ, it is the path to accumulate the strain hardening between habit planes generated by α activation. Because, depending on the initial OR between α/θ, the energy needs top form misfit dislocation can be higher, and the small misorientations angles can cause significant changes in the strain energy by change the magnitude of the burgers vector of the dislocations and their spacing as the heterophase boundary (K. Jaemin, 2016).

The stability of θ phase during stage II provided the strain hardening of α phase. After $\gamma = 0.21$, the components of the cementite are already well defined. It is interesting to note, the cementite keeping the same tendency to reorients to $\{001, 010\ \text{and}\ 100\}$ with the true shear strain evolution, but $\varphi 2 = 0°$, show the stability of $\{012\} < 13\ 8\ 4 >$, and these component

stay vary close to the initial $\{001\} < 14\ 9\ 0>$. However, A. Mussi (2016) reported that the transmission of plasticity into the cementite phase cane only be activated along of [010] direction for (100) plane. Reinforce this, the atomic simulations to cyclic deformation, showed occurrence of activation of ferrite slip systems, but no systems in cementite were activated (Lun-Wei Liang, 2020). For this, the orientation of lamellae cementite and direction of pearlite colony it must be taken into consideration. Due the heterogeneity of colonies, the change of θ orientation needs more studies.

A contribution of strain hardening arises because the change of lamellae texture will nucleate interfacial defects close the phase boundary. Analyzing influence of carbide in AISI 420 stainless steel, Changyu Wang (2022) reported, the carbide/matrix interface acts as an effective site of dislocation nucleation and obstacle to the dislocation movement. Nonetheless, this contribution of strain hardening will influence the crystallinity of θ. With the evolution of $\gamma = 0.31, 51$ and 53, deformation, the intensities of θ ODF go to higher in Fig. 11. Also, to Fig. 6c-d, reenforce that the amorphization for orthorhombic phase. Akira Taniama (2017), noted, that the increase of true strain, cementite fragments into small pieces and the change to amorphous cementite. That amorphization, is correlate to the vacancies generated by cementite decomposition, with this, the interfacial dislocations will annihilated and consequently relaxed the strain hardening in α/θ boundary (Y.T. Zhou, 2022). It should be noted, that the rotations of α phase in the $\gamma = 0.31$ is limited by θ, being that, cementite will pile up interfacial defects (Ning Guo, 2015; Mohammad Masoumi, 2022; Habib Sidhom, 2015; E. Gadalińska, 2020). Vaibhav N Khiratkar (2021) suggested that, the bending and fragmentation of cementite lamellae has better strain accommodation.

The change of texture, will forming the new interfaces formation energy, to the strain hardening. The amorphization of orthorhombic phase irises with high values of strain in α/θ interface, contributed to the mean free path, and defects will follow sub grains boundary, due the low interface energy for the new orientation relationship arising from the deformation of θ. With *In-Situ* Synchrotron tensile of hypereutectoid steel, M. L. Young (2007) using finite-element modeling, reported that, marked load transfer of α-Ferrite to the elastic Fe_3C particles. In the same perspective, E. Gadalińska (2020) founded that, both phases in pearlitic steel are loaded similary due to the equal elastic properties, but the plastic deformation leads to significant load transfer from ferrite top cementite. In Fig. 8e were indicate respectively the local meeting of dislocation parallel to lamellar pattern (BFTEM). The crack propagation in deformed cementite

into interface of activation slip system with the sub-grains highlighted with the yellow dotted line (Fig. 8f).

6. CONCLUSIONS

This study aimed to characterize the *In-Situ* crystallographic behavior of pure shear during uniaxial stress. With this, the texture of both phases was analyzed and used to explain the True Shear Stress x True Shear Strain curve of fully pearlitic steel. The initial orientation relationship between α/θ was observed and used to explain the changes on the phase boundary. The following conclusions were:

- The prior defects will give the energy to activated the slip system with the low Schmid factor.
- The strain hardening will rotate the less density atomic planes for those with greater crystallographic activation capabilities and the dislocation will follow the same or close the directions as the initial reflection, like $\{310\} < 131 >$ to $\{011\} < 522 >$ and $\{113\} < 152 >$ go to $\{112\} < 152 >$.
- The α/θ boundary will nucleate the interfacial defects and depends on the change in texture will influence of the strain hardening.
- The activation of θ dislocation will depend on the α activation.
- The new orientations far from {100, 010 and 001} will amorphized due to low interface energy thus allowing the formation of a high angle contour.

REFERENCES

A. Mussi, P. Cordiera, S. Ghoshb, N. Garvika, B. C. Nzoganga, Ph. Carreza and S. Garruchet, 2016. Transmission electron microscopy of dislocations in cementite deformed at high pressure and high temperature. PhilosoPhical Magazine 96, 1773-1789.

A.M. Elwazri, P. Wanjara, S. Yue, 2005. The effect of microstructural characteristics of pearlite on the mechanical properties of hypereutectoid steel. Mat. Science and Engineering 404, 91-98.

Akira Taniyama, Toru Takayama, Masahiro Arai, and Takanari Hamada, 2017. Deformation Behavior of Cementite in Deformed High Carbon Steel Observed by X-ray Diffraction with Synchrotron Radiation. The minerals, Metals & Materials Society 48A, 4821-4830

Anik H.M. Faisal, Christopher R. Weinberger, 2023. Nucleation of extrended defects in BCC transition metals. International Journal of Plasticity 170, 103742.

B. D. Cullity, S. R. Stock, 2001 . Elements of X-Ray Diffraction – Prentice Hall, 3rd edition,171-242.

By G. I. Taylor, F.R.S, 1934. The Mechanism of Plastic Deformation of Crystals - Part I.— Theoretical. Royal Society Yarrow Professor, 362-387.

C. P. L. Rodrigo, B. Miloslav, M. Mohammad, F. G. A. Hamilton, 2021. The effect of pearlite morphology and crystallographic texture on environmentally assisted cracking failure. Eng. Failure Analysis 126.

C. Du [1], F. Maresca [2], M.G.D. Geers, J.P.M. Hoefnagels, 2018. Ferrite slip system activation investigated by uniaxial micro-tensile tests and simulations. Acta Materialia 146, 314-327.

C. Lei, G. Masahide , H. Yoshiaki, H. Yukio, 2007. Effect of Microstructure of Cementite on Interphase Stress State in Carbon Steel. Journal of Iron and Steel Research, International 14, 31-38.

C.S. Pande, K.P. Cooper, 2009. Nanomechanics of Hall-Petch relationship in nanocrystalline materials. Progress in Materials Science 54, 689-706.

Changyu Wang, Kaiyu Luo, Jian Wang, Jinzhong Lu, 2022. Carbide-Facilitated nanocrystallization of martensitic laths and carbide deformation in AISI 420 stainless steel during laser shock peening. International Journal of Plasticity 150, 103191.

Christian Thiel, Jendrik Voss, Robert J. Martin, Patrizio Neff, 2019. Shear, pure and simple. International Journal of Non-Linear Mechanics 112, 57-72.

D.S. Zhou and G.J. Shiflet, 1992. Ferrite: Cementite Crystallography in Pearlite. Metallurgical Transactions A 23, 1259-1269.

Dan-dan Ma, Ping Yang, Xin-Fu Gu, Yusuke Onuki, Shigeo Sato, 2020. In-situ neutron diffraction investigation on the martensite transformation, texture evolution and martensite reversion in high manganese TRIP steel. Materials Characterization 163, 110244.

E. Gadalińska, A. Baczmański, C. Braham, G. Gonzalez, H. Sidhom, S. Wroński, T. Buslaps, K. Wierzbanowski, 2020. Stress localisation in lamellar cementite and ferrite during elastoplastic deformation of pearlitic steel studied using diffraction and modeling. International Journal of Plastice 127, 102651.

Fulin Jiang, Takuro Masumura, Kentaro Hirata, Toshihiro Tsuchiyama, Setsuo Takaki, 2019. A new diffraction line profile breadth analysis approach for evaluating plastic lattice strain anisotropy in cold-worked nickel under various strain paths. International Journal of Plasticity 112, 89-107.

George E. Dieter, 1981, Mecanical Metalurgy. 92-213, 282-331.

H. J. Bunge and C. Esling, 1982. Quantitative Texture Analysis. Deutsche Gesellschaft Fur Metallkunde E.V. And Société Française de Métallugie, 1-73.

H. K. D. H. Bhadeshia, 2018. Cementite. International Materials Reviews 65, 1-27.

H.J. Bunge. Texture Analysis in Materials Science Mathematical Methods, 1993. Cuvillier Verlag, 47-116.

Habib Sidhom, H. Yahyaoui, C. Braham, and G. Gonzalez, 2015. Analysis of the Deformation and Damage Mechanisms of Pearlitic Steel by EBSD and ‘‘in-situ’’ SEM Tensile Tests. Journal of Materials Engineering and Performance, 1059-9495.

Haimin Zhai, Xu Ma, Bo Cheng, Dongqing He, Xinjian Zhang, Wensheng Li, Chunling Li, Xiao song Li, Anhui Cai, 2022. Room temperature nanoindentation creep behavior of detonation sprayed Fe-based amorphous coating. Intermetallics 141, 107426.

Haitao Jiao, Yunbo Xu, Longzhi Zhao, R.D.K. Misra, Yanchuan Tang, Dejia Liu, Yong Hu, Min gjuan Zhao, Mingxue Shen, 2020. Texture evolution in twin-roll strip cast non-oriented electrical steel with strong cube and Goss texture. Acta Materialia 199, 311-325.

Hongqi Li, Hahn Choo, Yang Ren, Tarik A. Saleh, Ulrich Lienert, Peter K. Liaw, Fereshteh Ebrahimi, 2008. Strain-Dependent Deformation Behavior in Nanocrystalline Metals. Physical Review Letters 101, 015502.

Jaemin Kim, Keonwook Kang, Seunghwa Ryu, 2016. Characterization of the misfit dislocations at the ferrite/cementite interface in pearlitic steel: Na atomistic simulation study. International Journal of Plasticity 83, 302-312.

Jairo Alberto Muñoz, Tarek Khelfa, Alexander Komissarov, José-María Cabrera, 2021. Ductility and plasticity of ferritic-pearlitic steel after severe plastic deformation. Materials Science and Engineering 805, 140624.

K. Kitayama, C.N. Tomé, E.F. Rauch, J.J. Gracio, 4F. Barlat, 2013. A crystallographic dislocation model fo describing hardening of polycrystals during strain path changes. Application to low carbon steels. International Journal of Plasticity 46, 54-69.

K. Tao, J.C. Qiao, Q.F. He, K.K. Song, Y. Yang, 2021. Revealing the Structural Heterogeneity of Metallic Glass: Mechanical Spectroscopy and Nanoindentatio Experiments. International Journal of Mechanical Sciences 201, 106469.

L. B. McCusker, R. B. Von Dreele, D. E. Cox, D. Louër and P. Scardi, 1999. Rietveld refinement guidelines. Journal of Applied Crystallography 32, 36-50.

Leonid V. Azároff, 1968. Elements of X-ray crystallography, McGraw-Hill Book Company, 186-285.

Lichu Zhoua, Feng Fanga, Masayoshi Kumagai, Ed Pickering, Xiaodan Zhang, 2022. A modified pearlite microstructure to overcome the strength-plasticity trade-off of heavily drawn

pearlitic wire. Scripta Materialia 206, 114236.

Lun-Wei Liang, Shi-Cheng Dai, Yan Chen, Hai-Ying Wang, Yun-Jiang Wang, Lan-Hong Dai, 2023. Emergent failure transition of pearlitic steel at extremely high strain rates. Computational Materials Science 2019, 112005.

Lun-Wei Liang, Yun-Jiang Wang, Yan Chen, Hai-Ying Wang, Lan-Hong Dai, 2020. Dislocation nucleation and evolution at the ferrite-cementite interface under cyclic loadings. Acta Materialia 186, 267-277.

M. Nikolussi,a S.L. Shang,b T. Gressmann,a A. Leineweber,a,* E.J. Mittemeijer,a Y. Wangb and Z.-K. Liub, 2008. Extreme elastic anisotropy of cementite, Fe3C: First-principle calculations and experimental evidence. Scripta Materialia 59, 814-817.

M. Dollar, I.M. Bernstein, A.W. Thompson, 1988. Influence of deformation substructure on flow and fracture of fuly pearlitic steel. Acta Metallurgica 36. 311-320.

M.L. Young, J.D. Almer, M.R. Daymond, D.R. Haeffner, D.C. Dunand, 2007. Load partitioning between ferrite and cementite during elasto-plastic deformation of ultrahigh-carbon steel. Acta Materialia 55, 1999-2011.

Mehdi Sanjari, Youliang He, Erik J. Hilinski, Steve Yue, Leo A.I. Kestens, 2016. Development of the {113}〈uvw〉 texture during the annealing of a skew cold rolled non-oriented electrical steel. Scripta Materialia 124, 179-183.

Mengmeng Liu, Yuli Liu, Heng Li, 2022. Deformation mechanism of ferrite in a low carbon Al-killed steel: Slip behavior, grain boundary evolution and GND development. Materials Science and Engineering: A 842, 143093.

Michael Zelin, 2002. Microstructure evolution in pearlitic steels during wire drawing. Acta Materialia 50, 4431-4447.

Mohammad Masoumi , Miloslav Be´resˇ, Luis Flavio Gaspar Herculano, Rodrigo de Carvalho Paes Loureiro, and Hamilton Ferreira Gomes de Abreu, 2020. Microstructure and Crystallographic Texture Changes under torsion Loading of Pearlitic Steel Strips. Journal of Materials Engineering and Performance 29, 7250-7259.

Mohammad Masoumi, Rodrigo de Carvalho Paes Loureiro, Pedro Pinheiro, Jorge Luiz Cardoso, Miloslav Béreš, Hamilton Ferreira Gomes de Abreu, 2022. Effect of Pre-strain on Microstructure, Texture, and Strengthening of fully Pearlitic Steel. Journal of Materials Engineering and Performance 31, 4642-4654.

Ning Guo, Bo Song, Bing-Shu Wang, Qing Liu, 2015. Influence of Torsion Deformation on Textures of Cold Drawing Pearlitic Steel Wires. Acta Metall. Sin. 28, 707-714.

Ning Zhang, Ping Yang, Weimin Mao, 2016. {001}〈120〉−{113}〈361〉 recrystallization textures induced by initial {001} grains and related microstructure evolution in heavily rolled electrical steel. Materials Characterization 119, 225-232.

Pablo B.P. Leão, J.R. Barros Neto, Samuel Filgueiras Rodrigues, Ladislav Novotný, Jorge Luiz Cardoso, Luis Flavio Gaspar Herculano, Tiago Nunes Lima, Antonio J. Ramirez, Hamilton Ferreira G. de Abreu, 2023. In-situ tensile-shear teste in SEM and DIC analysis of two pearlitic stell microstructures: undeformed-coarse and deformed-refined. JMRT 24, 9441-9461.

Pablo B.P. Leão, Shutong Zhang, J.R. Barros Neto, Suyanny A. Freire, Rodrigo de C.P. Loureiro, Antonio J. Ramirez, H.F.G. de Abreu, 2023. Microstructure, microtexture, and crack susceptibility in pearlitic steel during lab-simulated process aiming tensile armor application in flexible pipelines. Journal of Materials Processing Technology 316, 117950.

Pedro Henrique Pinheiro Lima, Samille Krycia Bezerra de Lima, Maria Veronica Goncalves Rodrigues, Luis Flavio Gaspar Herculano, Rodrigo Carvalho de Paes Loureiro, Suyanny Assunção Freire, Jorge Luiz Cardoso, Mohammad Masoumi, Gedeon Silva Reis, Eden Santos Silva, Samuel Filgueiras Rodrigues, Hamilton Ferreira Gomes de Abreu, 2023. Assessing the influence of cyclic bending on pearlitic wire's microstructural evolution: a simulation of spiraling and armoring processing effects. JMRT 26, 1984-2000.

R. A. Young, 1993. The Rietveld Method. Oxford Science Publications, 43-166.

R. B. Von Dreele, 1997. Quantitative texture analysis by Rietveld refinement. Journal of Applied Crystallography 30, 517-525.

R.K.Ray, J.J.Jonas 1990. Transformation *textures* in steels. Int. Mate. Rev. 35, 1 – 36.

S. Suwas and S. Mondal, 2019. Texture Evolution in Severe Plastic Deformation Processes. Materials Transactions 60, 1457-1471.

S. Das Bakshi, D. Sinha, S. Ghosh Chowdhury, 2018. Anisotropic broadening of XRD peaks of α'-Fe: Williamson-Hall and Warren-Averbach analysis using full width at half maximum (FWHM) and integral breadth (IB). Materials Characterization 142, 144-153.

S. Suwas R. K. Ray, 2014. Crystallographic Texture of Materials. Springer London Heidelberg New York Dordrecht, pag. 11-37.

Steffen Scherbring, Bernhard Adms, Javad Mola, 2024. Impact of interlamellar spacing and non-pearlitic features on mechanical properties and cyclic damage initiation in near-euctetoid pearlitic steels. Materals Science & Engineering A 889, 145846.

T.Shinozaki, S.Morooka, T.Suzuki, Y.Tomota and T.Kamiyama, 2006. Influence of Lamellar Spacing on Deformation Behavior of Pearlite Steels Studied by ‘‘in-situ’’ Neutron Diffraction. In: The 3rd International Conference on Advanced Structural Steels Gyeongju, August 22-24.

Toshihiko Teshima, Makoto Kosaka, Kohsaku Ushioda, Norimitsu Koga, Nobuo Nakada, 2017. Local cementite cracking induced by heterogeneous plastic deformation in lamellar pearlite. Materials Science and Engineering: A 679, 223-229.

V. Randle, A. Olaf, 2010. Introduction to texture Analysis Macrotexture, Microtexture, and Orientation Mapping. Taylor & Francis Group, Second Edition, pag. 123-172.

Vaibhav N Khiratkar, Kushal Mishra, Aparna Singh, 2021. Deformation and microstructural evolution of nano-structured pearlite under tension versus torsion. Steel research international 92, 1-9.

William F. Hosford, 1993. The mechanics of crystals and textured polycrystals. Oxford University Press. Deformation Textures, 128-134.

William F. Hosford, 2010. Mechanical Behavior of Materials, Second Edition Cambridge, p.113-133.

Xingyang Tu, Xianbo Shi, Wei Yan, Changsheng Li, Quanqiang Shi, Yiyin Shan, Ke Yang, 2022. Tensile deformation behavior of ferrite-bainite dual-phase pipeline steel. Materials

Science and Engineering: A 831, 142230.

Y. Yasudaa, T. Ohashib, T .Shimokawaa and T. Niiyama, 2018. Strain-hardening characteristics of ferrite layers in pearlite microstructure. Materials Science and Technology 34, 772-779.

Y. Tian, H.T. Wang, Q.B. Ye, Q.H. Wang, Z.D. Wang, G.D. Wang, 2020. Effect of rolling reduction below γ non-recrystallization temperature on pancaked γ, microstructure, texture and low-temperature toughness fot hot rolled steel. Materials Science and Engineering: A 794, 139640.

Y.T. Zhou, X.H. Shao, S.J. Zheng, X.L. Ma, 2022. Structure evolution of the Fe_3C/Fe interface mediated by cementite decomposition in cold-deformed pearlitic steel wires. Journal of Materials Science & Technology 101, 28-36.

Yujiao Li, Dierk Raabe, Michael Herbig, Pyuck-Pa Choi, Shoji Goto, Aleksander Kostka, Hiroshi Yarita, Christine Borchers, and Reiner Kirchheim, 2014. Segregation Stabilizes Nanocrystalline Bulk Steel with Near Theoretical Strength. Physical Review Letters 113, 106104.

Zhang Yongtao, Han Haibo, Miao Lede, Zhang Hanqian, Li Jinfu, 2009. Quantitative carbide analysis using the Rietveld method for 2.25Cr-1Mo-0.25V steel. Materials Characterization 60, 953-956.

Zhaoyue Liu, Xianhui Wang, Ping Yang, Jiaji Ma, 2022. Different formation mechanism of {210}<001> orientation in η fiber texture of ultra-thin grain-oriented silicone steel using quase-in-situ analysis method. Materials Chemistry and Physics 278, 125726.

Zhenghua He, Jiande Liu, Xiaofei Zhu, Xinya Zhai, Yuhui Sha, Hongbo Hao, Lijia Chen, 2023. Secondary recrystallization of {310}<001> texture and enhanced magnetostriction in Fe-Ga alloy thin sheet. JMRT 22, 1868-1877.

Zifan Wang [a], Jingwei Chen [a], Oxana V. Magdysyuk [b], Fatih Uzun [a], Alexander M. Korsunsky, 2022. Ultra-fast quantification of polycrystalline texture via single shot synchrotron X-ray or neutron diffraction. Materials Characterization 186, 111827.